Improved magnetic circuit analysis of a laminated magnetorheological elastomer devices featuring both permanent magnets and electromagnets

Shaoqi Li[1], Peter A. Watterson[2], Yancheng Li[1,3*], Quan Wen[4], Jianchun Li[1]

1. School of Civil and Environmental Engineering, Faculty of Engineering and Information Technology, University of Technology Sydney, Ultimo, NSW 2007, Australia
2. School of Electrical and Data Engineering, Faculty of Engineering and Information Technology, University of Technology Sydney, Ultimo, NSW 2007, Australia
3. School of Civil Engineering, Nanjing Tech University, Nanjing 211816, China
4. School of Mechanical Engineering, Nanjing University of Science and Technology, Nanjing 210094, China

Email: Yancheng.li@uts.edu.au; Jianchun.li@uts.edu.au;

Abstract

As an essential and critical step, magnetic circuit modelling is usually implemented in the design of efficient and compact magnetorheological (MR) devices, such as MR dampers and MR elastomer isolators. Conventional magnetic circuit analysis simplifies the analysis by ignoring the magnetic flux leakage and magnetic fringing effect. These assumptions are sufficiently accurate in dealing with less complicated designs, featuring short magnetic path lengths such as in an MR damper. However, when dealing with MR elastomer devices, such simplification in magnetic circuit analysis results in inaccuracy of dimensioning and performance estimation of the devices due to their sophisticated design and complex magnetic paths. Modelling permanent magnets also imposes challenges in the magnetic circuit analysis. This work proposes an improved approach to include magnetic flux fringing effect in magnetic circuit analysis for MR elastomer devices. An MRE-based isolator containing multiple MRE layers and both a permanent magnet and an exciting coil was designed and built as a case study. The results of the proposed method are compared to

those of conventional magnetic circuit modelling, finite element analysis and experimental measurements to demonstrate the effectiveness of the proposed approach.

Keywords

Magnetorheological elastomer; magnetic circuit modelling; flux fringing effect; permanent magnet

1. Introduction

Dispersing ferromagnetic particles in elastomeric solids obtains a class of smart material normally termed magnetorheological elastomer (MRE) [1]. It exhibits a unique and useful phenomenon which is tunable material properties, i.e., stiffness and damping, upon the application of external magnetic field. Benefiting from this phenomenon, successfully applications have been reported in the fields of civil engineering [2,3] and mechanical engineering [4,5] for structural control and vibration reduction purposes; and, recently, its potentials have been further extended to developing sensors, robots and wearables [6-9].

One of the major branches of MRE-based application is isolators which can achieve adaptive isolation performance against different types of seismic conditions due to its tunable stiffness and damping [10]. Drawing on the design of commercial laminated rubber bearings, the multi-layer configuration is normally adopted in MRE isolators due to its excellence in carrying vertical loading with the minimal bulging effect in the elastomer layers. Li *et al*. developed the first adaptive base isolator with 47 layers of MRE [11]. Based on this configuration, Li *et al*. further improved the adaptive range of base isolators by developing a highly adjustable base isolator with 1630% increase of lateral stiffness [12]. Harnessing the benefits of this highly adjustable isolator, Gu *et al*. constructed a real-time controlled smart seismic isolation system and conducted a series of concept-proof experiments with sound outcomes [13]. Following these successful developments,

numerous researches on the multi-layer structured MRE isolators have been carried out. Xing *et al*. developed a novel base isolator with 20 layers of MRE [14]. Although these applications all achieve sound vibration mitigation performances, solely relying on electromagnet coils to provide magnetic field for the devices brings significant thermal and energy consumption issues [15]. In the applications for base isolators or bridge bearings where higher lateral stiffness is required to resist small disturbances like wind load and building live load in the majority of the service life, the coils in the device should be powered continuously [16]. Addressing these issues, the innovation of utilizing both electromagnet coils and permanent magnets (PM) has been proposed. The introduction of permanent magnets (PMs) provides MRE devices with a "bias" magnetic field present when the electric current is zero, which can reduce energy consumption. A positive or negative electric current can be applied to increase or decrease the magnetic field and tailor the device properties. For example, hybrid magnets laminated MRE adaptive isolators designed by Yang et al. [16] and Sun et al. [17] realized stiffness softening capability, maintaining stability without power during normal service life, and achieving effective base isolation during seismic events.

However, implementing the multi-layered structure and PM both adds difficulty and challenge to the design of device configuration and analysis of electromagnetic performance. For multi-layered structure, steel sheets with high relative permeability, which is normally around 5000, are chosen to bond with MRE layers to give a higher conductivity for magnetic field. However, the relative permeability of MRE is usually as low as 1 to 7 [18]. Laminating these two types of material may result in magnetic fluxes leaking out from high permeability layers, forming unpredicted flux paths and irregular flux density distributions in the multi-layer structure. As for using PM, the complexities lie in the inhomogeneous magnetic field distribution on the PM surfaces and the

prevention of irreversible demagnetization. Considering the strong magnetic field dependence of MR materials, revealing the magnetic field distribution inside of the laminated MRE devices featuring hybrid magnets is critical and mandatory to achieve cost-effective and reliable designs. However, this cannot be achieved by experimental methods, since current available magnetic field sensors are not capable of detecting the field distribution inside of a cured laminated structure without any structural modifications on the device. And opening slots on the laminated structure to accommodate the sensor will cause the detour of magnetic flux path and unreliable measurements.

Numerically, standard practice is to undertake the design using finite element software, such as ANSYS Maxwell or COMSOL Multiphysics. However, the construction of FEA models requires comprehensive details of the device which are commonly not available at the initial design stage. To obtain an optimal design of an MR device often involves numerous rounds of trial-and-error. Another analysis approach in developing magnetorheological (MR) devices, namely magnetic circuit modelling (MCM), produces equational presentations of the relationships between the device performance and variables such as the magnetic field strength, material properties and dimensions of the components. MCM allows theoretical, quantitative analysis and optimization focusing on predominant design parameters without involving much effort in modifying the geometry of the design and physical properties of the used materials in the first place. MCM has been successfully used in developing, analyzing and optimizing MR fluid dampers [19-25], MR fluid actuators [26-28] and MR fluid valves [29-32].

However, MR fluid devices and MRE devices should be treated separately when considering MCM as a design technique. For MR fluid devices, large damping force can be realized by controlling the flow of fluid through narrow channels permeated by the controllable magnetic field.

Therefore, the magnetic path of MR fluid devices is normally simple and of small length-scale. Simple device configurations result in homogeneous magnetic field distributions in the MR fluid. In such configurations, the standard MCM assumptions of no branched magnetic flux paths and no flux fringing are accurate, and thus the conventional MCM method is viable. However, making these assumptions can dramatically degrade the accuracy and reliability in designing MRE devices especially multilayer MRE devices which include larger length-scale and branched magnetic flux paths. In addition, unlike the sealed structure of MR fluid devices, air gaps and free spaces are usually allocated in MRE devices to avoid friction or collision of moveable parts during shear movements. The existence of air gaps introduces considerable flux fringing effect and imposes design challenges as a consequence. Furthermore, the multilayer structure of MRE devices results in inhomogeneous field distribution in the device. Wang et al. [33] suggested a design methodology incorporating finite element analysis (FEA) to design an MRE-based isolator featuring a ten-layered laminated conical-shaped core. The magnetic field analysis showed that the average magnetic flux density varied over a factor 2 between the top and middle layers of MRE. Xing et al. [34] also pointed out substantial differences of magnetic flux density at different locations in the laminated structure of an MRE bearing. The inhomogeneous distribution of magnetic flux density among MRE layers triggers different MR effects and causes discrepancies of mechanical performance of the devices. These phenomena suggest that the flux leakage and branched flux paths should be included in MCM for multilayer MRE devices. Though structural complexities of MRE devices imply challenges in implementing the MCM method, some pilot investigations have been conducted. Zhou [35] and Zhou et al. [36] iterated equational relationships between magnetic flux densities and device specifications of MRE shear testing rigs through MCM. Böse et al. [37] adopted MCM for evaluating the performance of an MRE valve. Yang et al. [38] computed the

magnetic field distribution of a shear-compression mixed mode MRE isolator by MCM and obtained close results to FEA. However, these existing MCM implementations for MRE devices made the same no flux-fringing assumptions as adopted for MR fluid devices and no multilayer MRE structures with a hybrid magnets configuration were investigated. Hence, practical guidance on developing MCM for hybrid magnets multi-layer MRE devices is of urgent demand.

In this work, an improved MCM approach to accurately analyze hybrid magnetic circuits involving laminated MRE materials is proposed. The new approach considers the magnetic flux fringing effect and branched magnetic flux paths and is therefore able to produce effective and efficient estimation of the magnetic field in the device with complicated structure. With revealing the equations of the relationships between device design parameters and magnetic flux density values, this approach also greatly avails the optimization process at the device design stage. A laminated MRE device featuring hybrid magnets was designed and manufactured as a benchmark case study. The accuracy of the proposed approach is validated via FEA results and experimental measurements.

2. Description of the benchmark device

Figure 1 shows the schematic diagram and a half of the section view with the illustration of the main flux paths of the proposed hybrid MRE isolator. The main body of the device adopts the proven design by Li et al. [11, 12] which is able to produce a good level of magnetic field across the MRE layers. That design is modified by the inclusion of a PM of thickness 5 mm and diameter 100 mm, sandwiched in the middle of the steel laminated MRE core. 9 layers of MRE and 9 layers of steel are laminated alternatively and bonded on both sides of the PM. The first layer attached to each of the two pole faces of the PM is steel. All steel and MRE layers are 1 mm thick. An air gap

of thickness 5 mm between the top plate and the yoke allows horizontal movement. Steel cylindrical blocks of height 37 mm were positioned between the MRE core and the top and bottom plates. Ten small coils, each having 350 turns, are stacked together and connected in parallel to a power supply. Detailed specifications for each component of the isolator are listed in Table 1.

Two magnetic field sources are specified in the device, namely the PM and the coil. When no current is applied to the coil, magnetic field is sourced from the PM. In this way, the MRE layers will maintain a higher stiffness without requiring any external electric power supplied to the device. The magnetic flux generated by the PM travels through the laminated MRE core, steel parts and the air gap, forming the major magnetic flux travel path. The intended current direction in the coil is such as to create magnetic flux opposing the magnetic flux generated by the PM hence reducing the magnetic flux densities in the MRE layers. The stiffness of the MRE material therefore decreases. Hence, softening and adaptability can be achieved by applying and varying the current supplied to the coil.

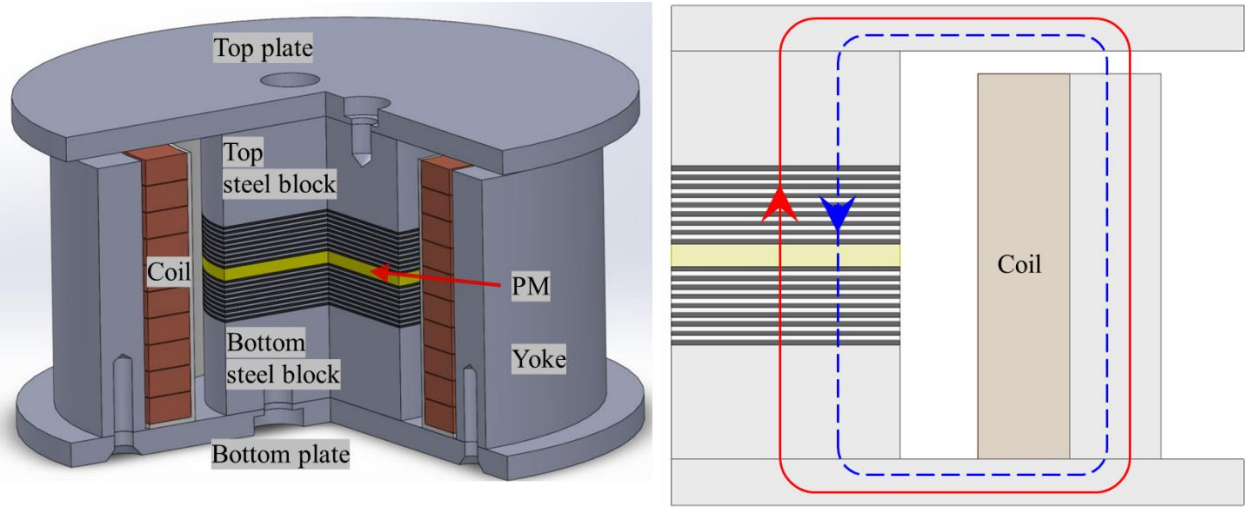

Figure 1. Overview and schematic (not to scale) of the proposed isolator. The fluxes generated by the coil and the PM are represented by the blue dashed line and the solid red line respectively.

Table 1. Specifications of the components of the isolator

	Material	Quantity	Axial Height (mm)	Diameter (mm)
Steel Block	Steel 1008	2	37	100
Steel Plate	Steel 1008	2	10	250
Yoke	Steel 1008	1	110	180 (inner); 220 (outer)
Steel Sheet	Steel 1008	18	1	100
MRE Sheet	MRE	18	1	100
PM	N40 NdFeB	1	5	100

3. Conventional MCM analysis

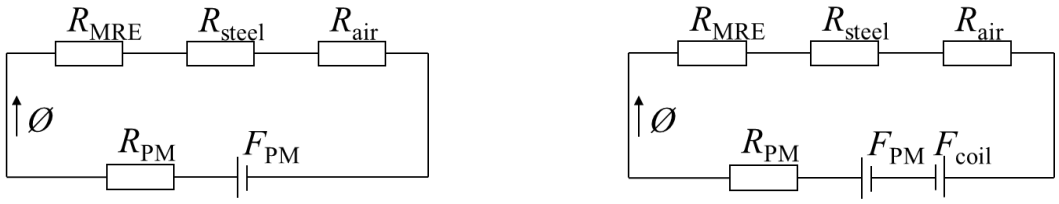

(a) Without current applied to coil (b) With current applied to coil

Figure 2. Magnetic circuit models without considering magnetic fringing

On the assumption that no fringing is considered, conventional MCM for the proposed isolator can be depicted as Figure 2. By assuming all components of the isolator are in series connection, the same flux travels through every part and is equivalent to the total flux $\emptyset$. The hybrid magnetic circuit, Figure 2(b), features the superposition of a magnetomotive force (MMF) from the PM, denoted F_{PM}, and an MMF from the coil, denoted F_{coil}, which operates in the opposite direction to that of F_{PM}. MMF values for PM and coil can be calculated by equation (1):

$$F_{\mathrm{PM}} = H_c l_{\mathrm{PM}}$$
$$F_{\mathrm{coil}} = Ni \tag{1}$$

where H_c is the coercivity of the PM, l_{PM} is the magnet thickness, N is the total number of turns of the coil, and i is the current in each turn. Since all components are in series, the total circuit reluctance is the sum of the reluctances for each type of material, R_{MRE}, R_{steel}, R_{airgap}, and R_{PM}, which are given by equation (2):

$$\begin{aligned} R_{\mathrm{MRE}} &= nl_{\mathrm{MRE}}/(\mu_{\mathrm{MRE}}A_{\mathrm{MRE}}) \\ R_{\mathrm{airgap}} &= l_{\mathrm{airgap}}/\,(\mu_{\mathrm{air}}A_{\mathrm{airgap}}) \\ R_{\mathrm{PM}} &= l_{\mathrm{PM}}/(\mu_{\mathrm{PM}}A_{\mathrm{PM}}) \\ R_{\mathrm{steel}} &= l_{\mathrm{yoke}}/(\mu_{\mathrm{yoke}}A_{\mathrm{yoke}}) + 2l_{\mathrm{plate}}/(\mu_{\mathrm{plate}}A_{\mathrm{plate}}) + \\ & 2l_{\mathrm{block}}/\,(\mu_{\mathrm{block}}A_{\mathrm{block}}) + nl_{\mathrm{steel\ sheet}}/(\mu_{\mathrm{steel\ sheet}}A_{\mathrm{steel\ sheet}}), \end{aligned} \tag{2}$$

where n is the total number of MRE layers, also equal the total number of steel sheet layers, l is the flux path length through each element, A is the flux cross-sectional area of each element, and $\mu = \frac{B}{H}$ is the element permeability, for H the magnetic field and B the magnetic flux density. For air, $\mu = \mu_0$. The N40 NdFeB magnet was assumed to have linear B-H curve in the second quadrant with remanence $B_{\mathrm{rem}} = 1.25$ T and coercivity $H_{\mathrm{c}} = 9.5 \times 10^5 \mathrm{Am}^{-1}$. The magnet is modelled as a cylindrical surface current of density H_{c} around the magnet perimeter with the interior of the magnet treated as having permeability $\mu_{\mathrm{PM}} = \frac{B_{\mathrm{rem}}}{H_{\mathrm{c}}} = 1.3158 \times 10^{-6}\mathrm{Hm}^{-1} = 1.047\mu_0$. The relationship between B and H for steel and MRE are presented in Figure 3 and symbolically expressed in equation (3):

$$\begin{aligned} H_{\mathrm{steel}} &= f_{\mathrm{steel}}(B_{\mathrm{steel}}) \\ H_{\mathrm{MRE}} &= f_{\mathrm{MRE}}(B_{\mathrm{MRE}}) \end{aligned} \tag{3}$$

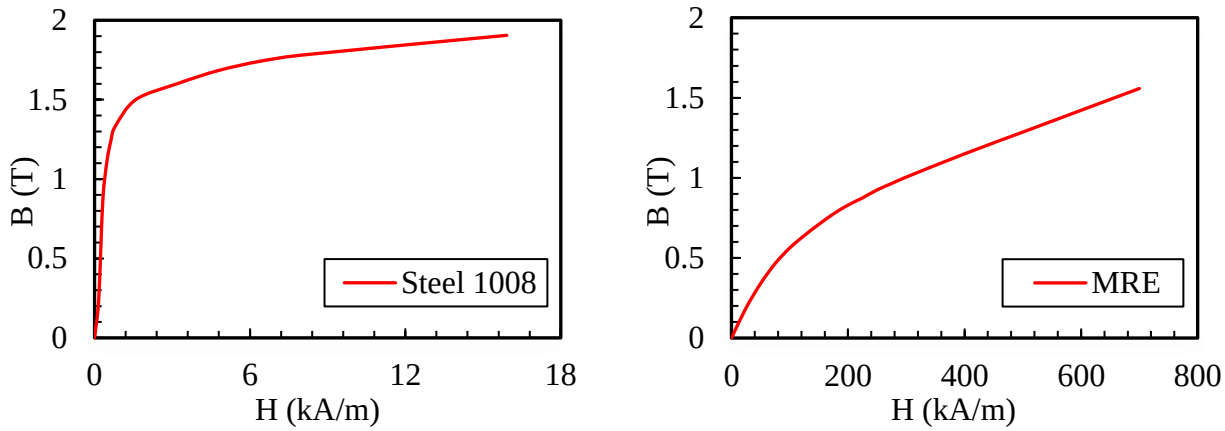

Figure 3. B-H curves for steel and MRE

B in each element is related to the flux and the element cross-sectional area by:

$$\emptyset = BA. \tag{4}$$

For the top and bottom plates of this circuit, A varies with radius. For the plate thickness chosen, the largest cylindrical cross-sectional area was smaller than the planar areas where the flux entered and exited the plate. The cylindrical cross-sectional area at the average of the inner yoke radius and the block outer radius was used. As a check against saturation, the MCM was repeated using the smallest area, at the block outer radius, and the results were found to change insignificantly. The calculations of the A and l values are specified in Appendix A.

The mathematical expressions of the magnetic circuit models constructed in Figure 2(a) and (b) can be expressed as equation (5) and (6), respectively:

$$F_{\text{pm}} = H_c l_{\text{PM}} = \sum f_{\text{steel}} \left(\frac{\emptyset}{A_i}\right) l_i + \sum f_{\text{MRE}} \left(\frac{\emptyset}{A_i}\right) l_i + \frac{\emptyset l_{\text{airgap}}}{\mu_{\text{air}} A_{\text{airgap}}} + \frac{\emptyset l_{\text{PM}}}{\mu_{\text{PM}} A_{\text{PM}}} \tag{5}$$

$$F_{\mathrm{pm}} - F_{\mathrm{coil}} = H_c l_{\mathrm{PM}} - Ni$$
$$= \sum f_{\mathrm{steel}} \left(\frac{\emptyset}{A_i}\right) l_i + \sum f_{\mathrm{MRE}} \left(\frac{\emptyset}{A_i}\right) l_i + \frac{\emptyset l_{\mathrm{air}}}{\mu_{\mathrm{air}} A_{\mathrm{airgap}}} + \frac{\emptyset l_{\mathrm{PM}}}{\mu_{\mathrm{PM}} A_{\mathrm{PM}}} \quad (6)$$

By substituting specifications and dimensions of each part of the isolator, the main flux $\emptyset$ is obtained and can be converted to magnetic flux densities distributed in each element through equation (4). Summarising Appendix A, Table 2 lists the MCM parameters of the isolator elements.

Table 2 Conventional MCM parameters for the MRE isolator

	n	*l* (mm)	*A* (mm^2)
Steel Block	2	37	7853.98
Steel Plate	2	110	4398.23
Yoke	1	110	12566.37
Steel Sheet	18	1	7853.98
MRE Sheet	18	1	7853.98
Air Gap	1	5	12566.37
PM	1	5	7853.98

Results from the conventional MCM for current applied to each small coil ranging from 0 A to 1.357 A are presented in Figure 4. The magnetic flux densities in all MRE layers is seen to decrease from 0.49 T to 0 T when the applied *i* increased from 0 A to 1.357 A. For the total number of turns N = 3500, 1.357 A current gives 4750 Aturns MMF of the ten coils (where Aturns is the product of the current times the number of turns) which is equal to the MMF of the PM, $H_{\mathrm{c}} l_{\mathrm{PM}}$, therefore, at this current, the magnetic field of the PM is cancelled out theoretically by the field generated by the coil. Although this method provides rapid solutions for estimating electromagnetic properties, the assumptions include ignoring the flux leakage and fringing effects; hence the amount of flux travelling throughout the entire circuit model is constant and flux density values are identical for

components sharing the same A value. Hence, for the laminated core area, flux density values in MRE sheets and steel sheets are the same, which is an inaccurate description of the magnetic flux density distribution for devices featuring laminated cores.

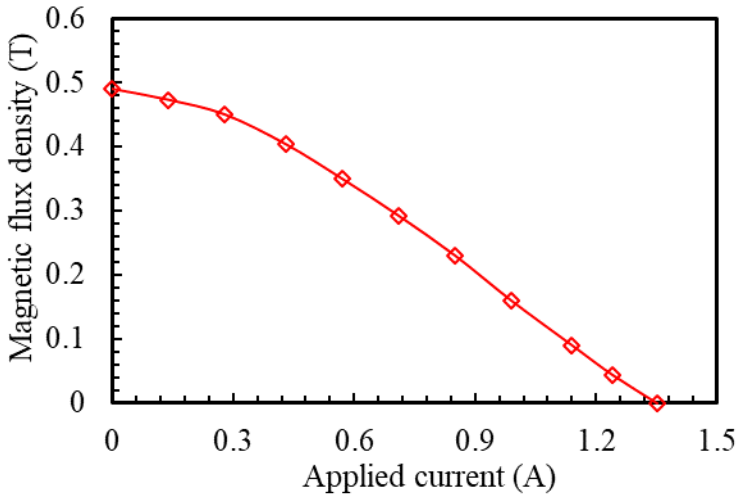

Figure 4. Magnetic flux density in MRE from MCM without considering fringing effect

4. FEA results

An axisymmetric finite element model of the prototype hybrid magnetic isolator was constructed and analysed through ANSYS Electronic Desktop. The software solved for the azimuthal component of the magnetic vector potential. Isotropic permeability was assumed for all materials. The N40 NdFeB magnet was assumed to have linear B-H curve in the second quadrant with remanence $B_{\text{rem}} = 1.25$ T and coercivity $H_c = 9.5 \times 10^5 \text{Am}^{-1}$. Solutions for current applied to each small coil, i, ranging from 0 A up to 1.357 A, at values corresponding to current MMF values 0 Aturns, 1000 Aturns, 2000 Aturns, 3000 Aturns, 4000 Aturns and 4750 Aturns, were computed in Figure 5. Due to the axial symmetry of the device, ½-axisymmetric presentations of the magnetic

flux density (B) plots are shown. Figure 5 (a) shows the B plot for 0 A in the coil, i.e. with the PM as the magnetic source. Magnetic flux fringing can be clearly observed at the air gap and around the laminated core area. Figure 5 (b)-(f) show the results as the *i* increases up to 1.357 A.

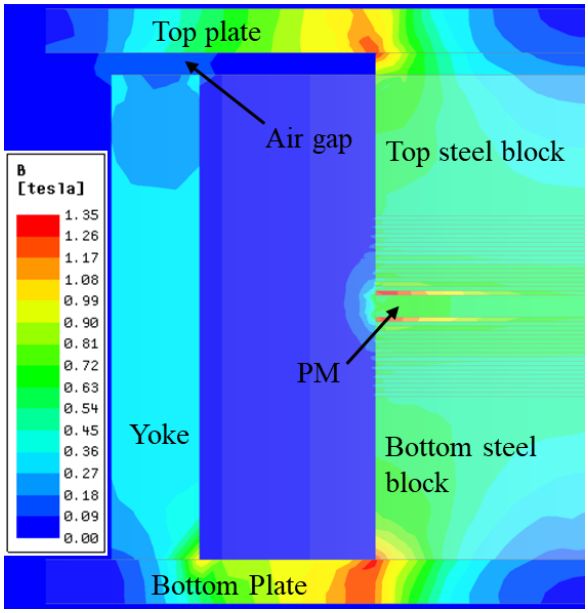

(a) $i = 0$ A

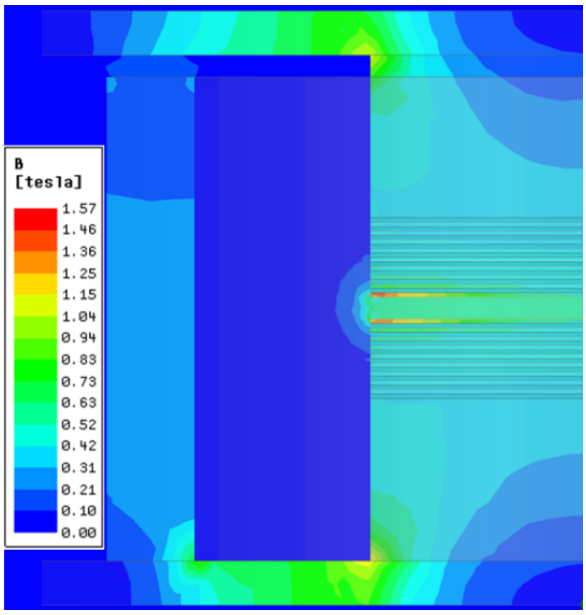

(b) $i = 0.286$ A

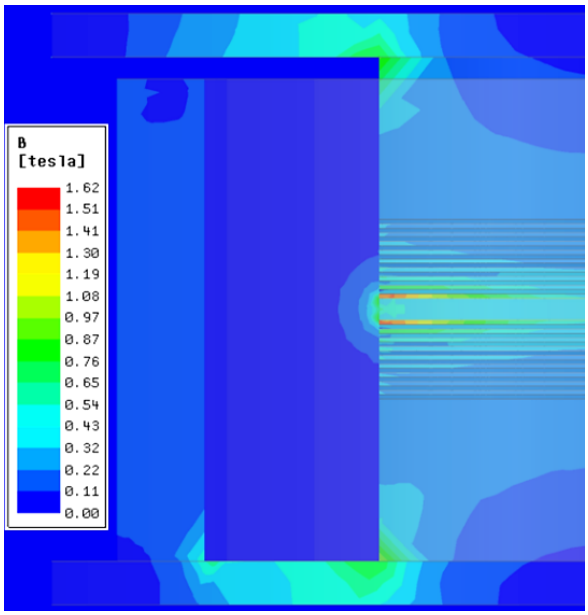

(c) $i = 0.571$ A

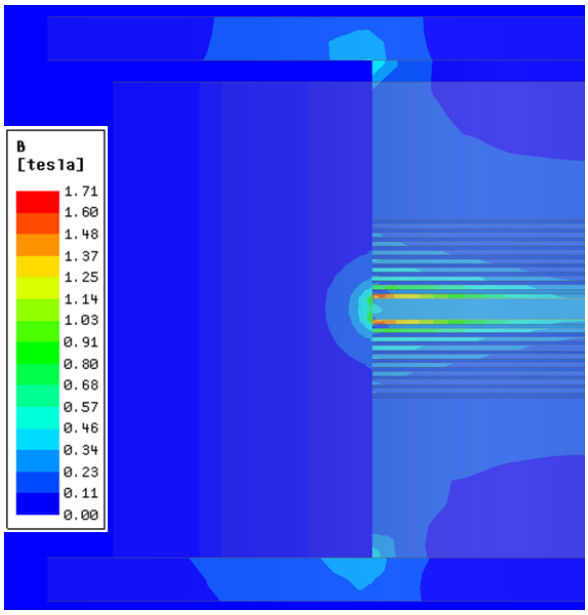

(d) $i = 0.857$ A

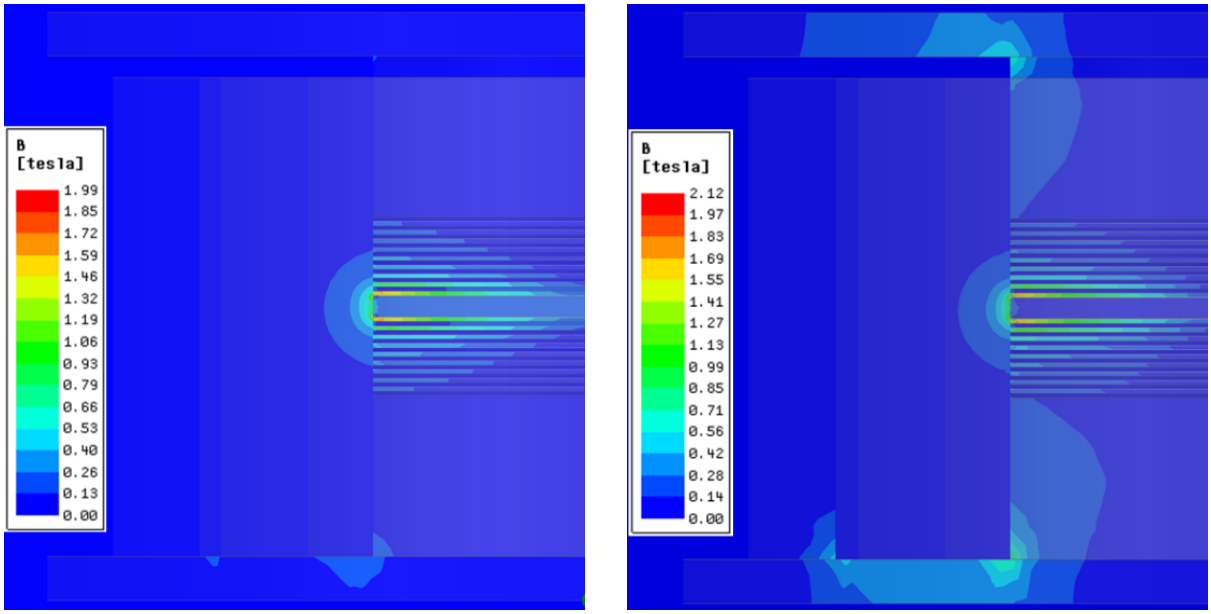

(e) $i = 1.143$ A (f) $i = 1.357$ A

Figure 5. Magnetic flux density plot from FEA

The FEA-calculated average flux density in each layer of the laminated core structure with different i applied is presented numerically in Table 3. The top MRE and steel sheets (furthest from the magnet on the air gap side) are numbered as the 9th layer and marked as M9 and S9 respectively. For zero current, the average magnetic flux density in the MRE layers decreases with distance away from the PM, falling from 0.58 T in the first MRE layer near the PM to 0.51 T in the furthest MRE layer from the PM. By comparing the FEA results with results from conventional MCM analysis, four major discrepancies are observed:

- The conventional MCM analysis only produces the amount of total flux travelling through the single flux path. The elements sharing the same cross-sectional area have the same flux density under these assumptions. For zero current in the coil, that B value is 0.49 T for every layer of the core structure including steel sheets, MRE sheets and PM. However, FEA showed an inhomogeneous distribution of magnetic flux density, with average B value varying from 0.63 T in the PM layer to 0.51 T in the top MRE layer.

- The conventional MCM analysis cannot capture the vector property of magnetic flux density. For example, in FEA, high magnetic flux densities were observed in the 1st and 2nd steel layers, namely 1.04 T and 0.70 T respectively. These values are unusual according to the conventional MCM since the flux density produced within the PM is 0.63 T. However, the explanation lies in the vector property of magnetic field: besides the longitudinal magnetic flux density component, there are the fringing magnetic fluxes leaking along the radial direction of the steel layers and the 1 mm thickness gives a narrow magnetic flux path. As a result, the small amount of fringing flux produces a high radial flux density component which contributes to produce high total magnetic flux density values in the steel layers. Within each MRE sheet, the flux density is nearly all longitudinal and is close to uniform in amplitude across the layer. However, in the steel sheets, the high permeability allows the flux a low reluctance radial path to the outer perimeter of the sheet and, especially for the 1st and 2nd steel sheets, a short leakage flux path to the other side of the PM.
- When the applied current in the coil increases to the equivalent amount of F_{PM}, the coil offsets the net magnetic flux density to 0 T everywhere in the conventional MCM. However, the FEA shows that in fact a flux density of 0.11 T remains in the PM. Associated with the magnetic fringing flux, the average flux density values in the 1st and 2nd steel layers still remained as high as for zero current in the coil.
- Flux fringing can also be observed at the air gap between the top plate and the yoke. In conventional MCM, the air gap is represented by a cylindrical annulus with the same inner and outer diametric as the yoke. However, as shown in the FEA magnetic flux density plot, instead of travelling straight across the modelled air gap, the flux fringes to

a larger area. Referring to equation (2), this will result in an error in estimating the reluctance of the air gap and therefore output an unreliable MCM result.

Table 3 Average flux densities (T) in each layer of the core structure

	0 A	0.286 A	0.571 A	0.857 A	1.143 A	1.357 A
M9	0.51	0.40	0.28	0.14	0.00	0.10
S9	0.51	0.40	0.29	0.17	0.10	0.15
M8	0.51	0.40	0.28	0.15	0.01	0.09
S8	0.52	0.41	0.30	0.19	0.12	0.17
M7	0.51	0.40	0.28	0.15	0.02	0.09
S7	0.52	0.42	0.31	0.21	0.15	0.18
M6	0.52	0.41	0.29	0.16	0.03	0.08
S6	0.53	0.43	0.33	0.23	0.18	0.20
M5	0.52	0.42	0.30	0.17	0.04	0.06
S5	0.55	0.45	0.35	0.27	0.22	0.24
M4	0.53	0.43	0.31	0.18	0.05	0.05
S4	0.57	0.48	0.39	0.31	0.28	0.30
M3	0.54	0.44	0.32	0.20	0.07	0.04
S3	0.60	0.53	0.45	0.41	0.40	0.42
M2	0.56	0.45	0.34	0.21	0.09	0.02
S2	0.70	0.66	0.62	0.67	0.71	0.75
M2	0.58	0.47	0.36	0.24	0.12	0.04
S1	1.04	1.02	0.99	1.03	1.02	1.04
PM	0.63	0.54	0.43	0.32	0.20	0.11

5. The proposed MCM analysis

The discrepancies above originate from the overly simplified assumptions adopted, such as single magnetic path with no fringing, simple air gap path, etc. A modified approach should be constructed in order to obtain more accurate magnetic field distributions. In the following, several modifications are applied in the proposed MCM, including modelling flux fringing in the air gap and around the magnet.

5.1 Modelling of the air gap

Referring to the equation (2) to (5), due to the low permeability of air, the estimation made of the air gap cross-sectional area can dramatically affect the accuracy of the MCM. A smaller air gap cross sectional area leads to a higher reluctance value of the air gap element and a lower total amount of flux. In the conventional MCM, the magnetic flux is assumed to travel through the air gap along the shortest path, i.e. on straight field lines. However, as shown in Figure 5(a), the flux travels in an expanded area between the top plate and the yoke. The flux travel path at the air gap is observed to be about 10 mm wider than the thickness of the yoke. This matches closely with the air gap model proposed by Roters [39] which is shown in Figure 6(a). In his model, the width of air gap element between two steel poles of equal width is extended for two times the gap height g. Although the greater lateral extent of the top plate would increase the actual air gap enlargement somewhat, the same enlargement of the air gap width on each side by the gap height g is assumed for the prototype isolator, as illustrated as Figure 6(b). Since the yoke is a tubular component, the air gap should also be modelled as tubular and its cross-sectional area can be formulated as follows in terms of the yoke inner and outer diameters:

$$A_{\text{airgap}} = \pi \times \left(\frac{\emptyset_{\text{yoke outer}}}{2} + g \right)^2 - \pi \times \left(\frac{\emptyset_{\text{yoke inner}}}{2} - g \right)^2 \tag{7}$$

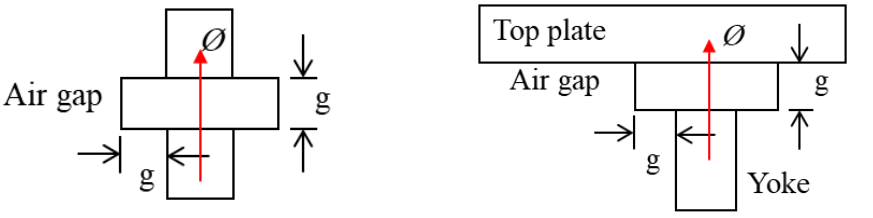

(a) Air gap model proposed by Roters [39]

(b) Air gap model for the proposed isolator

Figure 6. Air gap models

5.2 MCM with consideration of flux fringing

In addition to the modified air gap model, the modelling of the laminated core structure is also improved in the proposed MCM method. Considering the vector property of magnetic flux, the fluxes dispersed in each cylindrical layer in the laminated core structure can be categorised into two dimensions which are normal flux ($\emptyset$) and radial flux ($\emptyset$') as shown in Figure 7. Normal flux is taken as the flux passing across the disk top surface of each element while radial flux is the flux leaked out through the side surface of the element in the radial direction. By the principle of magnetic flux conservation, the difference of the fluxes crossing the top and bottom surfaces of a layer must equal the flux leaked out the side of the layer. Because the permeability of MRE is much lower than that of steel and the radial path across the sheets is quite long, the radial flux leakage for the MRE sheets is ignored, i.e. approximated as 0. The difference in $\emptyset$ between the adjacent MRE layers equals the $\emptyset$' of the steel layer in between them. Denoting the total amount of flux generated by the PM, the normal flux in the i^{th} MRE layer and the leakage flux in the i^{th} steel layer are denoted as $\emptyset_{PM}$, $\emptyset_i$ and $\emptyset'_i$ respectively, their relationships are represented as equation (8):

$$\begin{aligned} \emptyset_{PM} &= \emptyset_1 + \emptyset'_1 \\ \emptyset_i &= \emptyset_{i+1} + \emptyset'_{i+1} \end{aligned} \tag{8}$$

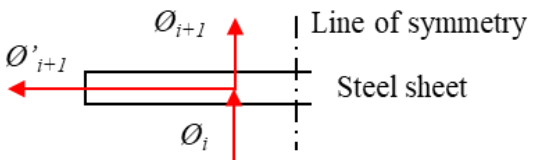

Figure 7. Normal flux and radial flux (distributed around the disc perimeter)

Accordingly, the proposed MCM is constructed and shown in Figure 8. Since fringing flux is neglected in all MRE layers, there is only one category of flux component for MRE layers which

is $Ø_i$. In steel layers, the magnetic flux was separated into two components which are the normal flux ($Ø_i$) and fringing flux ($Ø'_i$). These fringing fluxes leak out at the i^{th} steel layers then travels through the air path which has the reluctance of R_{airi} and goes back to the laminated structure forming the paralleled air reluctance elements in the circuit. The illustration for the flux leakage paths, i.e., R_{air1} and R_{air2}, are presented in Figure 9. The calculation of R_{airi} values follows equation (2). In equation (2), l used is the length of path which crosses the centre of the cross section of R_{airi} (presented as red dotted line in Figure 9); and, A is using the cylindrical surface area of the steel sheet. Since the fringing fluxes leaked out from steel sheet layers in the radial direction, the radial reluctance of steel sheet (R_{sr}) is also include in the paralleled fringing path. R_{airi} values are summarised in Appendix B. R_{sz} is the reluctance of steel sheet in the normal direction. Assuming the flux leakage only occurs at the middle point of the axial height of the steel sheet, for $Ø_{PM}$ and $Ø_9$, they only travel for the half of the 1st and 9th steel sheets respectively on the normal direction.

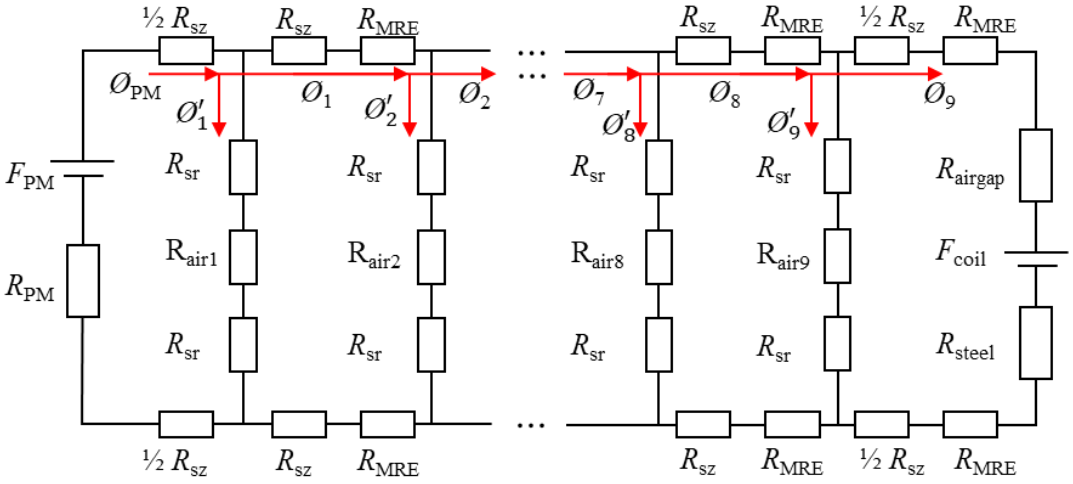

Figure 8. MCM with considering Magnetic flux fringing effect

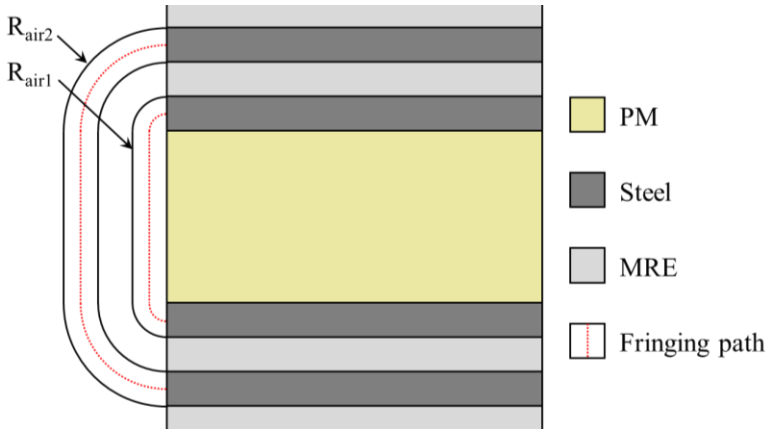

Figure 9. Flux leakage path

Additionally, to include the influence of fringing flux at air gap between the top plate and the yoke, the air gap model presented in Figure 6(b) and equation (7) was adopted in this MCM to provide a more accurate cross-sectional size for air gap. Following Kirchhoff's law, the mathematical expression of the proposed MCM can be expressed as equation (9):

$$\begin{aligned} F_{\mathrm{PM}} &= \emptyset_{\mathrm{PM}}\left(R_{\mathrm{PM}} + R_{\mathrm{SZ}}\right) + \emptyset_1'\left(2R_{\mathrm{SR}} + R_{\mathrm{air1}}\right) \\ \emptyset_1'\left(2R_{\mathrm{SR}} + R_{\mathrm{air1}}\right) &= \emptyset_2'\left(2R_{\mathrm{SR}} + R_{\mathrm{air2}}\right) + 2\emptyset_1\left(R_{\mathrm{MRE}} + R_{\mathrm{SZ}}\right) \\ \emptyset_i'\left(2R_{\mathrm{SR}} + R_{\mathrm{air}i}\right) &= \emptyset_{i+1}'\left(2R_{\mathrm{SR}} + R_{\mathrm{air}i+1}\right) + 2\emptyset_i\left(R_{\mathrm{MRE}} + R_{\mathrm{SZ}}\right) \\ F_{\mathrm{coil}} &= -\emptyset_9\left(R_{SZ} + 2R_{\mathrm{MRE}} + R_{airgap} + R_{Steel}\right) + \emptyset_9'\left(2R_{\mathrm{SR}} + R_{\mathrm{air9}}\right) \end{aligned} \tag{9}$$

By substituting equation (2), (3) and (8) into equation (9), the amount of flux in each layer can be yielded. To simplify the solving procedure, permeability for steel and MRE is assumed as constant with $\mu_{steel} = 3.93 \times 10^{-3}$ Hm^{-1} and $\mu_{MRE} = 4.73 \times 10^{-6}$ Hm^{-1}. This assumption is valid since the flux densities in all steel components did not reach saturation; as for MRE, the total axial height of MRE sheets is small, i.e., 18 mm, which has insignificant influence on the result accuracy.

However, the flux density cannot be obtained through Gauss' Law directly, since the fluxes in the normal and radial direction for each element should all be considered when calculating flux density. Considering the vector property of magnetic field, equation (10) should be adopted to obtain the flux density in steel sheet.

$$B = \sqrt[2]{(\emptyset_i/A_n)^2 + (\emptyset_i'/A_r)^2} \tag{10}$$

Where A_n and A_r are the areas of the top surface and the side surface of the steel sheet.

6. Results and Discussion

The computed flux density at each layer using FEA, MCM and MCM considering flux fringing (MCMF) effect is illustrated in Figure 10. The horizontal axis represents the layers of the laminated core. The results from conventional MCM are represented by the flat grey lines since this method cannot capture the variances of magnetic field in laminated core structures. The red bar and black bar represent the results from the improved MCM and FEA. The green line and blue line indicate the errors of the MCM with considering flux fringing effect and the conventional MCM compared with FEA in percentage which are calculated through equation (11). Detailed values of magnetic flux densities and errors are summarised in Table 4.

$$Error = \frac{ABS(model\ result - FEA\ result)}{FEA\ result} \times 100\% \tag{11}$$

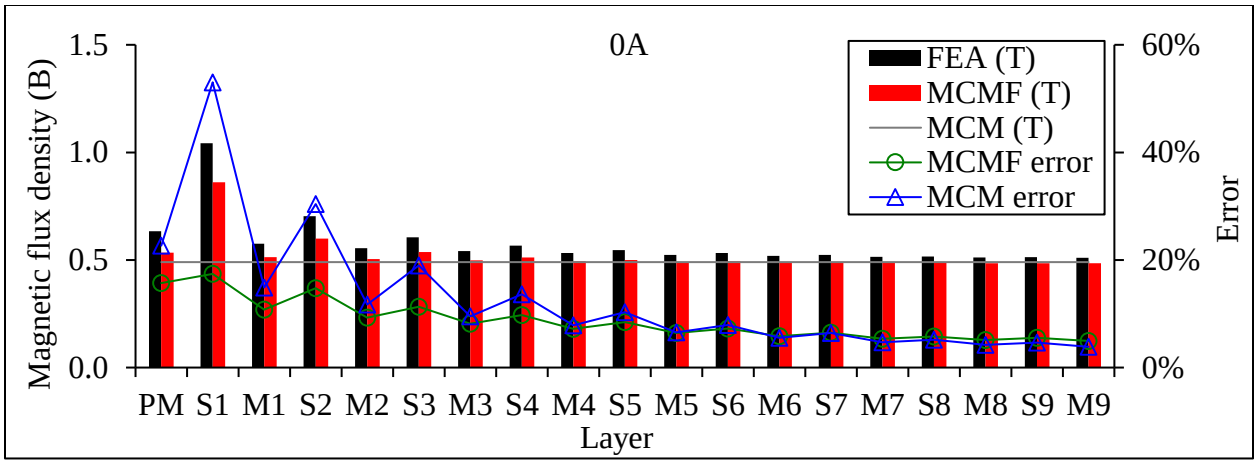

(a) $i = 0$ A

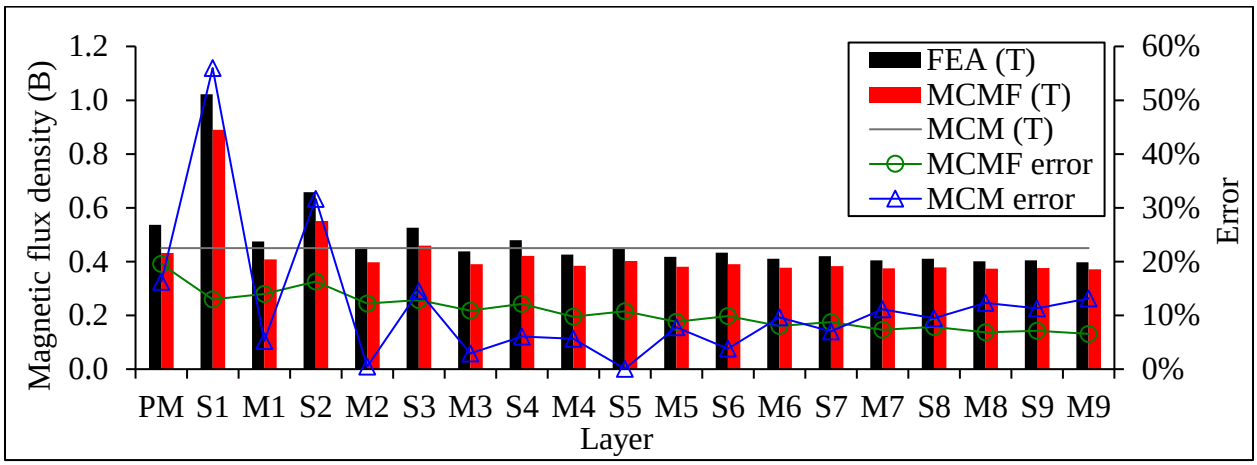

(b) $i = 0.286$ A

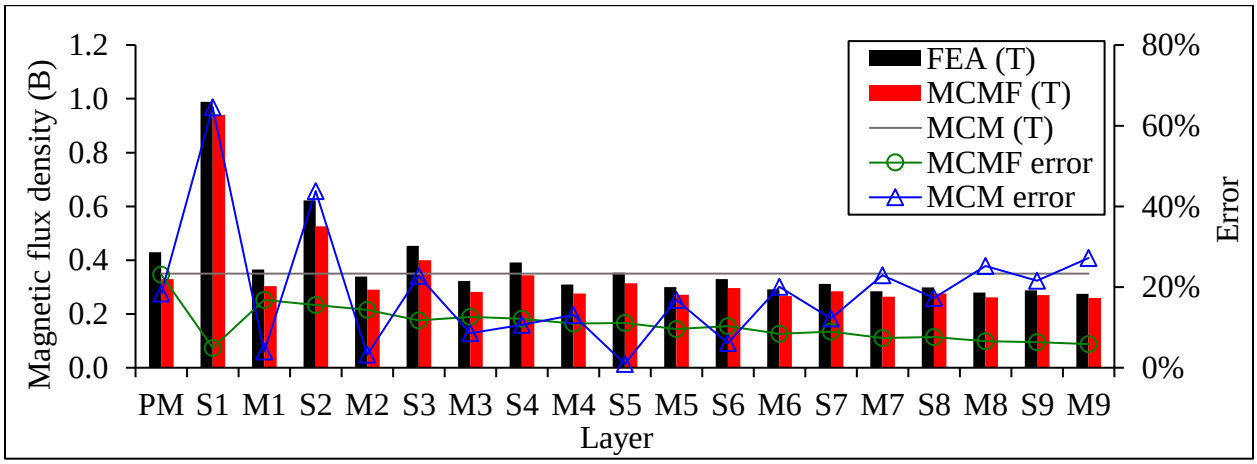

(c) $i = 0.571$ A

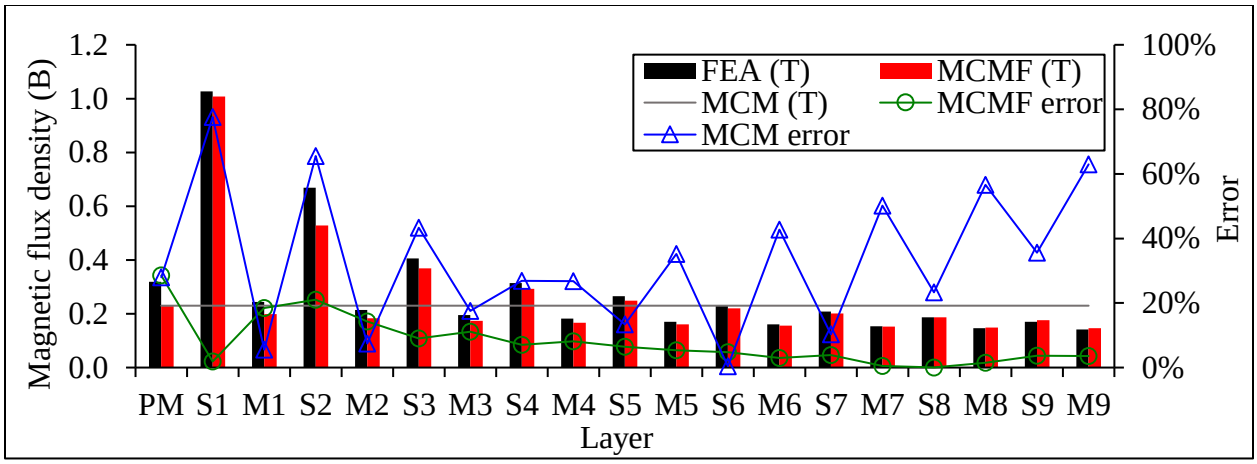

(d) i = 0.857 A

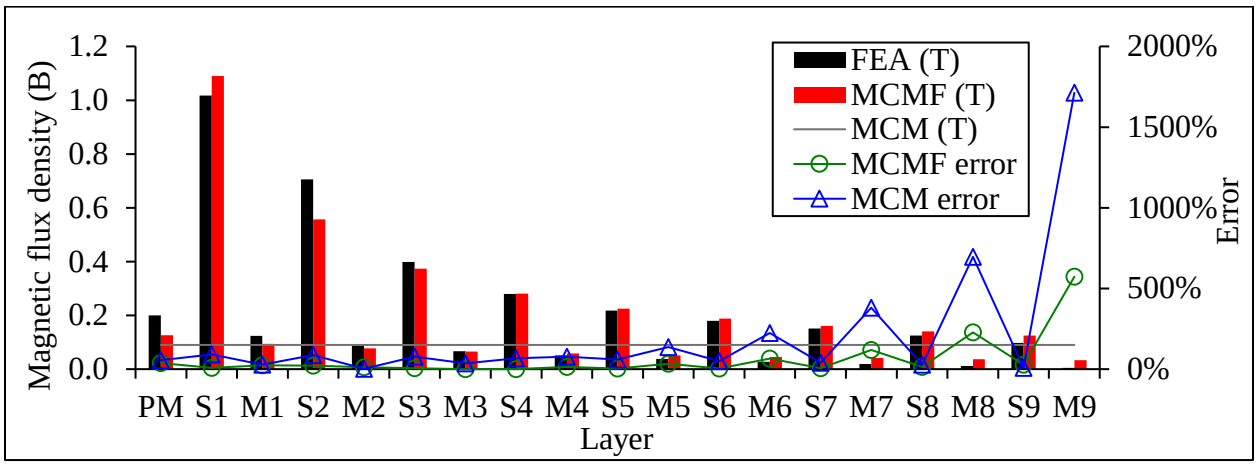

(e) i = 1.143 A

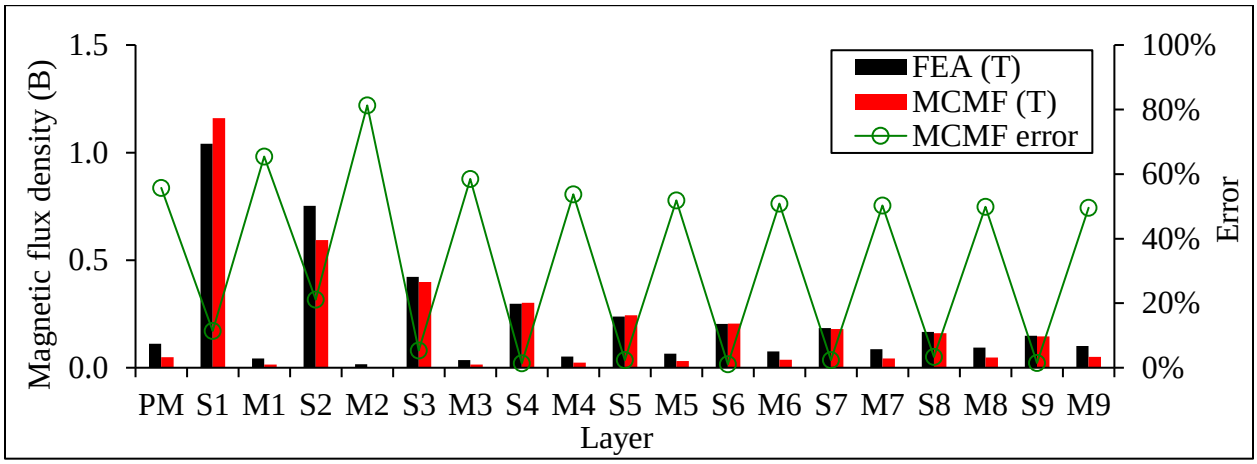

(f) i = 1.357 A

Figure 10. Computed flux density for each layer of the laminated structure when different i applied using FEA, MCM and MCMF (MCM considering fringing effect)

Table 4 Results from FEA, MCM and MCMF (MCM considering fringing effect)

(a) i = 0 A					
	FEA (T)	MCMF (T)	MCM (T)	MCMF error	MCM error
PM	0.63	0.53	0.49	15.7%	22.7%
S1	1.04	0.86	0.49	17.4%	53.0%
M1	0.58	0.51	0.49	10.8%	14.8%
S2	0.70	0.60	0.49	14.8%	30.4%
M2	0.56	0.50	0.49	9.3%	11.7%
S3	0.60	0.54	0.49	11.3%	19.0%
M3	0.54	0.50	0.49	8.1%	9.5%
S4	0.57	0.51	0.49	9.7%	13.6%
M4	0.53	0.49	0.49	7.2%	7.8%
S5	0.55	0.50	0.49	8.4%	10.3%
M5	0.52	0.49	0.49	6.4%	6.5%
S6	0.53	0.49	0.49	7.2%	7.9%
M6	0.52	0.49	0.49	5.9%	5.5%
S7	0.52	0.49	0.49	6.5%	6.4%
M7	0.51	0.49	0.49	5.4%	4.7%
S8	0.52	0.49	0.49	5.7%	5.2%
M8	0.51	0.49	0.49	5.1%	4.2%
S9	0.51	0.49	0.49	5.5%	4.6%
M9	0.51	0.48	0.49	4.9%	3.9%

(b) i = 0.286 A					
	FEA (T)	MCMF (T)	MCM (T)	MCMF error	MCM error
PM	0.54	0.43	0.45	19.6%	16.2%
S1	1.02	0.89	0.45	13.0%	56.0%
M1	0.47	0.41	0.45	14.0%	5.2%
S2	0.66	0.55	0.45	16.3%	31.6%
M2	0.45	0.40	0.45	12.2%	0.5%
S3	0.53	0.46	0.45	12.9%	14.5%
M3	0.44	0.39	0.45	10.9%	2.9%
S4	0.48	0.42	0.45	12.1%	6.1%
M4	0.43	0.38	0.45	9.7%	5.6%
S5	0.45	0.40	0.45	10.8%	0.1%
M5	0.42	0.38	0.45	8.8%	7.8%
S6	0.43	0.39	0.45	9.9%	3.8%
M6	0.41	0.38	0.45	8.0%	9.6%
S7	0.42	0.38	0.45	8.7%	7.0%
M7	0.40	0.38	0.45	7.3%	11.1%
S8	0.41	0.38	0.45	7.8%	9.5%
M8	0.40	0.37	0.45	6.8%	12.3%
S9	0.40	0.38	0.45	7.1%	11.3%
M9	0.40	0.37	0.45	6.6%	13.1%

(c) i = 0.571 A					
	FEA (T)	MCMF (T)	MCM (T)	MCMF error	MCM error
PM	0.43	0.33	0.35	23.1%	18.4%
S1	0.99	0.94	0.35	4.9%	64.6%
M1	0.36	0.30	0.35	16.8%	4.1%
S2	0.62	0.53	0.35	15.5%	43.8%
M2	0.34	0.29	0.35	14.3%	3.3%
S3	0.45	0.40	0.35	11.7%	22.8%
M3	0.32	0.28	0.35	12.6%	8.6%
S4	0.39	0.34	0.35	12.1%	10.6%
M4	0.31	0.28	0.35	11.0%	13.1%
S5	0.35	0.31	0.35	11.1%	1.0%
M5	0.30	0.27	0.35	9.6%	16.8%
S6	0.33	0.30	0.35	10.3%	6.1%
M6	0.29	0.27	0.35	8.4%	20.1%
S7	0.31	0.28	0.35	8.9%	12.2%
M7	0.28	0.26	0.35	7.4%	22.9%
S8	0.30	0.28	0.35	7.6%	17.3%
M8	0.28	0.26	0.35	6.5%	25.2%
S9	0.29	0.27	0.35	6.3%	21.6%
M9	0.28	0.26	0.35	5.9%	27.2%

(d) i = 0.857 A					
	FEA (T)	MCMF (T)	MCM (T)	MCMF error	MCM error
PM	0.32	0.23	0.23	28.5%	27.9%
S1	1.03	1.01	0.23	1.9%	77.6%
M1	0.24	0.20	0.23	18.5%	5.5%
S2	0.67	0.53	0.23	21.0%	65.6%
M2	0.21	0.18	0.23	14.2%	7.4%
S3	0.41	0.37	0.23	9.0%	43.3%
M3	0.20	0.17	0.23	11.1%	17.6%
S4	0.31	0.29	0.23	7.0%	26.9%
M4	0.18	0.17	0.23	8.2%	26.7%
S5	0.27	0.25	0.23	6.5%	13.4%
M5	0.17	0.16	0.23	5.4%	35.2%
S6	0.23	0.22	0.23	4.7%	0.4%
M6	0.16	0.16	0.23	2.9%	42.8%
S7	0.21	0.20	0.23	3.8%	10.3%
M7	0.15	0.15	0.23	0.5%	50.1%
S8	0.19	0.19	0.23	0.0%	23.3%
M8	0.15	0.15	0.23	1.5%	56.6%
S9	0.17	0.18	0.23	3.7%	35.6%
M9	0.14	0.15	0.23	3.5%	62.9%

(e) i = 1.143 A					
	FEA (T)	MCMF (T)	MCM (T)	MCMF error	MCM error
PM	0.20	0.13	0.09	37.0%	55.1%
S1	1.02	1.09	0.09	7.2%	91.1%
M1	0.12	0.09	0.09	24.4%	27.3%
S2	0.71	0.56	0.09	21.1%	87.2%
M2	0.09	0.08	0.09	12.3%	2.5%
S3	0.40	0.37	0.09	6.2%	77.4%
M3	0.07	0.07	0.09	0.9%	35.1%
S4	0.28	0.28	0.09	0.5%	67.8%
M4	0.05	0.06	0.09	13.7%	77.2%
S5	0.22	0.23	0.09	3.1%	58.8%
M5	0.04	0.05	0.09	34.1%	135.9%
S6	0.18	0.19	0.09	4.5%	49.9%
M6	0.03	0.05	0.09	65.1%	224.9%
S7	0.15	0.16	0.09	6.6%	40.3%
M7	0.02	0.04	0.09	119.2%	380.4%
S8	0.12	0.14	0.09	13.0%	27.6%
M8	0.01	0.04	0.09	227.2%	695.9%
S9	0.10	0.12	0.09	28.2%	7.4%
M9	0.00	0.03	0.09	572.5%	1712.5%

(f) i = 1.357 A					
	FEA (T)	MCMF (T)	MCM (T)	MCMF error	MCM error
PM	0.11	0.05	0.00	55.7%	
S1	1.04	1.16	0.00	11.4%	
M1	0.04	0.01	0.00	65.4%	
S2	0.75	0.59	0.00	21.2%	
M2	0.02	0.00	0.00	81.3%	
S3	0.42	0.40	0.00	5.4%	
M3	0.04	0.01	0.00	58.5%	
S4	0.30	0.30	0.00	1.4%	
M4	0.05	0.02	0.00	53.8%	
S5	0.24	0.24	0.00	2.3%	Not applicable
M5	0.06	0.03	0.00	51.9%	
S6	0.20	0.21	0.00	1.1%	
M6	0.08	0.04	0.00	50.9%	
S7	0.18	0.18	0.00	2.4%	
M7	0.09	0.04	0.00	50.3%	
S8	0.17	0.16	0.00	3.3%	
M8	0.09	0.05	0.00	49.9%	
S9	0.15	0.15	0.00	1.5%	
M9	0.10	0.05	0.00	49.6%	

As shown in Figure 10(a), for the scenario with no current applied, the overall error for all layers of the laminated core obtained from the proposed MCM and the conventional MCM are 8.71% and 12.73%. The proposed MCM can well portray the variance of magnetic field in different layers and the excessively high flux density values in the first 3 steel layers which are 1.02 T, 0.78 T and 0.64 T respectively, with error within 12%. For MRE layers, the average error of the proposed MCM is 7.02%. The maximum and minimum flux density values in MRE are 0.51 T and 0.48 T for the 1st and the 9th MRE layers well matched with FEA results. The maximum error of flux densities value between the proposed MCM and FEA is only 0.18 T, however, that of the conventional MCM is 0.55 T.

By increasing the applied i to 1.143 A, as illustrated in Figure 10(e), the overall error of the proposed MCM increased to 63.00%. Nevertheless, the overall error of conventional MCM soared to 202.86%. The magnetic flux density in the PM was effectively reduced from 0.53 T to 0.13 T when the applied i increased from 0 to 1.143 A, according to the improved MCM. At this scenario, although the percentage error increased due to the decrease of base number, the maximum error of flux density value between the improved MCM and FEA is only of 0.15 T (0.93 T for the conventional method). It can be concluded that the improved MCM can effectively capture the electromagnetic performance of the device when different i is applied.

With the increase of the applied current to the coil, the flux density in MRE layers decreases, however, flux fringing effect at the laminated core still exhibits eminent flux density values in the steel layers. Additionally, the difference between flux densities of steel and MRE layers became more noticeable when larger current was applied, especially for the layer adjacent to the PM. The computed improved MCM can well reproduce this behaviour. For example, for the first steel layer,

it yields 0.86 T, 0.89 T, 0.93 T, 1.01 T and 1.09 T for applied *i* increased from 0 A to 1.143 A with the overall error less than 9%. On the contrary, conventional MCM reached almost 70% error for these five scenarios. With further increase of the applied current to 1.357 A, which is the scenario that the conventional MCM failed to compute, the proposed MCM still achieves a high accuracy with overall percentage error of 32% and maximum error of flux density value of 0.16 T.

Compared with available results from FEA and the conventional MCM, the effectiveness and superiority of the proposed MCM in depicting the magnetic flux density for the hybrid magnets laminated core and flux fringing effect have been revealed.

7. Further discussion

7.1 Experimental validation of magnetic field

In the real design of laminated MRE-based adaptive devices, currently, the magnetic field in the laminated structure can only be estimated by FEA and MCM; and, there is no sensor available to directly measure the field distribution inside of a laminated structure without damaging the structure and changing the flux path. Therefore, developing a rapid and accurate MCM is of great significance addressing the structural complexity of laminated MRE-based devices.

A prototype hybrid magnets isolator was manufactured; and, magnetic field measurement was carried out to prove the reliability of the proposed MCM. The measurement locations were at the middle of the gap between the top plate and the yoke, as indicated in Figure 11, since these locations are in the magnetic flux path and can accommodate a gauss meter probe. Figure 12 shows the setup of the measurement. The isolator was powered by HDS800PS30 power supply (Helios, Australia) configured in AMP-K6030 rack (Helios, Australia). The gauss meter is TM-197 (Tenmars, Taiwan).

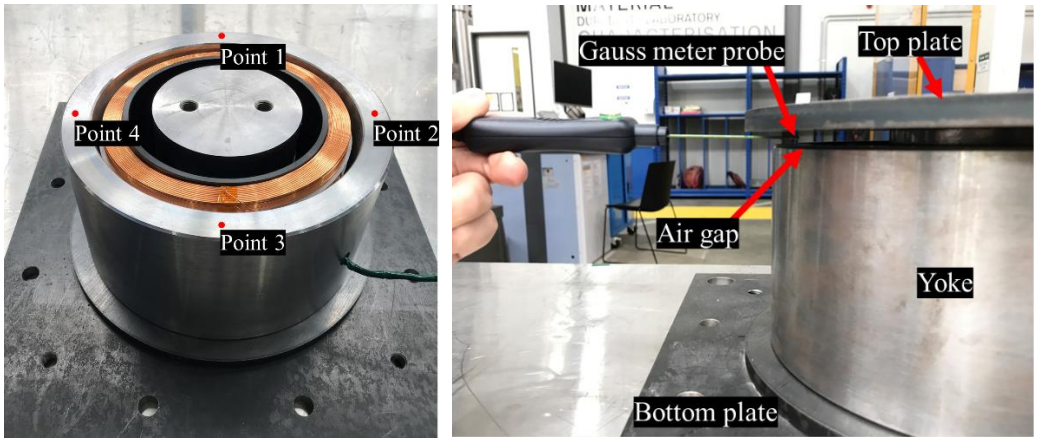

Figure 11. Measurement positions

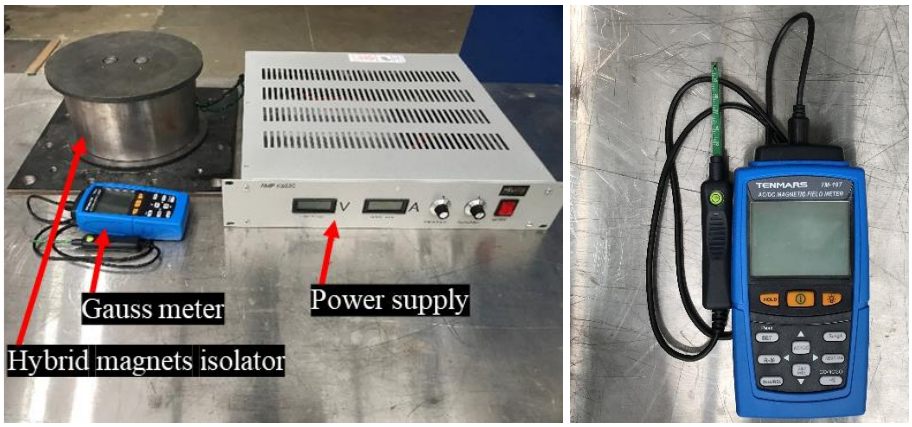

Figure 12. Measurement setup and gaussmeter

The measured magnetic flux density values are summarised in Table 5. The average measured flux density of the four locations and the results of flux density in the air gap from the improved MCM and FEA results are plotted in Figure 13. The FEA results were taken at the middle point of the top plate and the yoke. The measured value is lower than both the FEA result and the improved MCM. A similar phenomenon has been reported by Li *et al* [11]. The major reason of having lower experimental values is that the bonding surfaces of the laminated structure were not considered in theoretical methods. The bonding of the MRE and steel layers in the real device is not as perfect as that in theoretical methods. In the 37-layer structure, there are 38 layers of adhesive applied and

the glue and air bubbles may not have been sufficiently removed between the MRE and steel layers in the laminated structure, which may have caused this discrepancy. Although differences exist, the trends of flux density in the air gap are similar among the three groups of results when the applied current is changing. The flux densities decrease with the increase of applied current linearly to the minimum value when 1.143 A applied; then start to increase with the increase of applied current.

Table 5 Measured flux density (mT) at the four points in the air gap

	Point 1	Point 2	Point 3	Point 4	Average
0 A	141.6	117.2	136.8	126.0	130.4
0.286 A	89.7	78.9	84.8	95.6	87.3
0.571 A	57.9	50.0	56.4	49.5	53.5
0.857 A	35.3	27.5	21.1	18.2	25.5
1.143 A	33.4	20.1	15.7	15.2	21.1
1.357 A	43.7	41.2	38.8	29.4	38.3

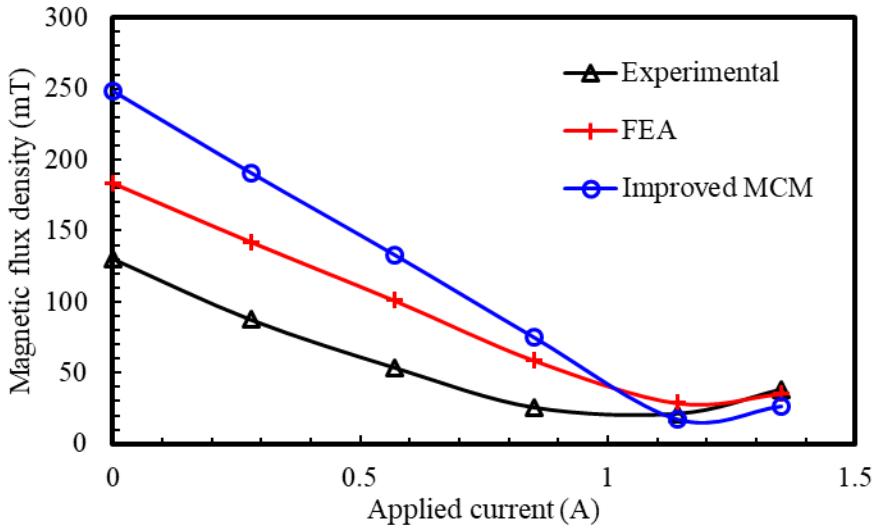

Figure 13. Comparison of experimental, FEA and the improved MCM results

7.2 Recommendations on the design of isolator with hybrid magnetic

As for optimization of hybrid magnet systems in the adaptive isolators with laminated MRE core structure, the selection and positioning of the PM and the configuration of coil are critical. For PM, according to suggestions from [40], realising the maximum magnetic energy product is preferred in order to make the volume of PM smallest and to give the highest efficacy of electromagnetic performance of the device. For a neodymium magnet, since its demagnetization curve is a straight line in the second quadrant, the max magnetic energy product can be reached when the magnetic flux density in the magnet is half of its remanence. According to the improved MCM, in the prototype device, the magnetic flux density in the PM is 0.61 T when no current applied to the coil. Since this value is around half of the remanence of an N40 neodymium magnet, e.g. 1.25 T, this device accomplished a most effective and compact configuration. Regarding the positioning of the PM, the design proposed used one layer in the middle of the laminated core structure rather than separating the PM into several thinner layers. This is to protect the PM from irrecoverable demagnetization when the coil is energised and also to avoid cracking of PM due to its brittle nature. The design of the coil should provide sufficient MMF to offset the magnetic field from the PM.

8. Summary

In this work, a novel MRE-based adaptive isolator featuring stiffness softening effect and an improved MCM has been proposed. Also, suggestions addressing the application of the hybrid magnet system were provided. Considering the magnetic field dependence of this device, theoretical analysis including conventional MCM and FEA have been conducted. FEA results revealed that the proposed device provides a wide range of controllability of magnetic field, which

can be offset to almost 0 T from 0.57 T in MRE layers when 1.357 A is applied to each small coil, therefore offering outstanding adjustability in the mechanical properties. By addressing the flux fringing effects the proposed MCM achieves excellence in capturing the magnetic field distribution localized to each layer in the laminated structure for both non-current applied and large current applied scenarios. The proposed MCM also mitigated the failure of computing the maximum current applied scenario for the conventional MCM.

Reference

[1] Ginder, J. M., Clark, S. M., Schlotter, W. F., & Nichols, M. E. (2002). Magnetostrictive phenomena in magnetorheological elastomers. *International Journal of Modern Physics B*, *16*(17n18), 2412-2418.

[2] Behrooz, M., Wang, X., & Gordaninejad, F. (2014). Performance of a new magnetorheological elastomer isolation system. *Smart Materials and Structures*, *23*(4), 045014.

[3] Jung, H. J., Eem, S. H., Jang, D. D., & Koo, J. H. (2011). Seismic performance analysis of a smart base-isolation system considering dynamics of MR elastomers. *Journal of Intelligent Material Systems and Structures*, *22*(13), 1439-1450.

[4] Ginder, J. M., Schlotter, W. F., & Nichols, M. E. (2001, July). Magnetorheological elastomers in tunable vibration absorbers. In *Smart Structures and Materials 2001: Damping and Isolation* (Vol. 4331, pp. 103-110). International Society for Optics and Photonics.

[5] Xu, Z., Gong, X., Liao, G., & Chen, X. (2010). An active-damping-compensated magnetorheological elastomer adaptive tuned vibration absorber. *Journal of Intelligent Material Systems and Structures*, *21*(10), 1039-1047.

[6] Yun, G., Tang, S. Y., Sun, S., Yuan, D., Zhao, Q., Deng, L., ... & Li, W. (2019). Liquid metal-filled magnetorheological elastomer with positive piezoconductivity. *Nature Communications*, *10*(1), 1300.

[7] Qi, S., Guo, H., Chen, J., Fu, J., Hu, C., Yu, M., & Wang, Z. L. (2018). Magnetorheological elastomers enabled high-sensitive self-powered tribo-sensor for magnetic field detection. *Nanoscale*, *10*(10), 4745-4752.

[8] Thorsteinsson, F., Gudmundsson, I., & Lecomte, C. (2015). *U.S. Patent No. 9,078,734*. Washington, DC: U.S. Patent and Trademark Office.

[9] Yang, T., Xie, D., Li, Z., & Zhu, H. (2017). Recent advances in wearable tactile sensors: Materials, sensing mechanisms, and device performance. *Materials Science and Engineering: R: Reports*, *115*, 1-37.

[10] Li, Y., & Li, J. (2019). Overview of the development of smart base isolation system featuring magnetorheological elastomer. *Smart Structures and Systems*, *24*(1), 37-52.

[11] Li, Y., Li, J., Li, W., & Samali, B. (2013). Development and characterization of a magnetorheological elastomer based adaptive seismic isolator. *Smart Materials and Structures*, *22*(3), 035005.

[12] Li, Y., Li, J., Tian, T., & Li, W. (2013). A highly adjustable magnetorheological elastomer base isolator for applications of real-time adaptive control. *Smart Materials and Structures*, *22*(9), 095020.

[13] Gu, X., Li, J., & Li, Y. (2020). Experimental realisation of the real‐time controlled smart magnetorheological elastomer seismic isolation system with shake table. *Structural Control and Health Monitoring*, *27*(1), e2476.

[14] Xing, Z. W., Yu, M., Fu, J., Wang, Y., & Zhao, L. J. (2015). A laminated magnetorheological elastomer bearing prototype for seismic mitigation of bridge superstructures. *Journal of Intelligent Material Systems and Structures*, *26*(14), 1818-1825.

[15] Yu, M., Zhao, L., Fu, J., & Zhu, M. (2016). Thermal effects on the laminated magnetorheological elastomer isolator. *Smart Materials and Structures*, *25*(11), 115039.

[16] Yang, J., Sun, S. S., Du, H., Li, W. H., Alici, G., & Deng, H. X. (2014). A novel magnetorheological elastomer isolator with negative changing stiffness for vibration reduction. *Smart Materials and Structures*, 23(10), 105023.

[17] Sun, S., Deng, H., Yang, J., Li, W., Du, H., Alici, G., & Nakano, M. (2015). An adaptive tuned vibration absorber based on multilayered MR elastomers. *Smart Materials and Structures*, 24(4), 045045.

[18] Kashima, S., Miyasaka, F., & Hirata, K. (2012). Novel soft actuator using magnetorheological elastomer. *IEEE Transactions on Magnetics*, *48*(4), 1649-1652.

[19] Yang, G., Spencer Jr, B. F., Carlson, J. D., & Sain, M. K. (2002). Large-scale MR fluid dampers: modeling and dynamic performance considerations. *Engineering Structures*, *24*(3), 309-323.

[20] Chen, C., & Liao, W. H. (2012). A self-sensing magnetorheological damper with power generation. *Smart Materials and Structures*, *21*(2), 025014.

[21] Milecki, A. (2001). Investigation and control of magneto–rheological fluid dampers. *International Journal of Machine Tools and Manufacture*, *41*(3), 379-391.

[22] Zheng, J., Li, Z., Koo, J., & Wang, J. (2014). Magnetic circuit design and multiphysics analysis of a novel MR damper for applications under high velocity. *Advances in Mechanical Engineering*, *6*, 402501.

[23] Zhu, X., Jing, X., & Cheng, L. (2012). Magnetorheological fluid dampers: a review on structure design and analysis. *Journal of Intelligent Material Systems and Structures*, *23*(8), 839-873.

[24] Yang, B., Luo, J., & Dong, L. (2010). Magnetic circuit FEM analysis and optimum design for MR damper. *International Journal of Applied Electromagnetics and Mechanics*, *33*(1-2), 207-216.

[25] Gavin, H., Hoagg, J., & Dobossy, M. (2001, August). Optimal design of MR dampers. In *Proceedings of the US-Japan Workshop on Smart Structures for Improved Seismic Performance in Urban Regions* (Vol. 14, pp. 225-236).

[26] Takesue, N., Furusho, J., & Kiyota, Y. (2004). Fast response MR-fluid actuator. *JSME International Journal Series C Mechanical Systems, Machine Elements and Manufacturing*, *47*(3), 783-791.

[27] An, J., & Kwon, D. S. (2003). Modeling of a magnetorheological actuator including magnetic hysteresis. *Journal of Intelligent Material Systems and Structures*, *14*(9), 541-550.

[28] Boelter, R., & Janocha, H. (1997, May). Design rules for MR fluid actuators in different working modes. In *Smart Structures and Materials 1997: Passive Damping and Isolation* (Vol. 3045, pp. 148-160). International Society for Optics and Photonics.

[29] Yoo, J. H., & Wereley, N. M. (2002). Design of a high-efficiency magnetorheological valve. *Journal of Intelligent Material Systems and Structures*, *13*(10), 679-685.

[30] Grunwald, A., & Olabi, A. G. (2008). Design of magneto-rheological (MR) valve. *Sensors and Actuators A: Physical*, *148*(1), 211-223.

[31] Guo, N. Q., Du, H., & Li, W. H. (2003). Finite element analysis and simulation evaluation of a magnetorheological valve. *The International Journal of Advanced Manufacturing Technology*, *21*(6), 438-445.

[32] Nguyen, Q. H., Han, Y. M., Choi, S. B., & Wereley, N. M. (2007). Geometry optimization of MR valves constrained in a specific volume using the finite element method. *Smart Materials and Structures*, *16*(6), 2242.

[33] Wang, Q., Dong, X., Li, L., & Ou, J. (2018). Mechanical modeling for magnetorheological elastomer isolators based on constitutive equations and electromagnetic analysis. *Smart Materials and Structures*, 27(6), 065017.

[34] Xing, Z. W., Yu, M., Fu, J., Wang, Y., & Zhao, L. J. (2015). A laminated magnetorheological elastomer bearing prototype for seismic mitigation of bridge superstructures. *Journal of Intelligent Material Systems and Structures*, 26(14), 1818-1825.

[35] Zhou, G. Y. (2003). Shear properties of a magnetorheological elastomer. *Smart Materials and Structures*, *12*(1), 139.

[36] Zhou, G. Y., & Li, J. R. (2003). Dynamic behavior of a magnetorheological elastomer under uniaxial deformation: I. Experiment. *Smart Materials and Structures*, *12*(6), 859.

[37] Böse, H., Rabindranath, R., & Ehrlich, J. (2012). Soft magnetorheological elastomers as new actuators for valves. *Journal of Intelligent Material Systems and Structures*, *23*(9), 989-994.

[38] Yang, C. Y., Fu, J., Yu, M., Zheng, X., & Ju, B. X. (2015). A new magnetorheological elastomer isolator in shear–compression mixed mode. *Journal of Intelligent Material Systems and Structures*, *26*(10), 1290-1300.

[39] Roters, H. C. (1941). *Electromagnetic devices*. Wiley.

[40] Wright, W., & McCaig, M. (1977). *Permanent Magnets*. Oxford University Press for the Design Council, the British Standards Institution, and the Council of Engineering Institutions.

Appendix A

$l_{\text{air}} = height\ of\ airgap = 5$ mm

$l_{\text{MRE}} = thickness\ of\ MRE = 1$ mm

$l_{\text{Steel sheet}} = thickness\ of\ steel\ sheet = 1$ mm

$l_{\text{Steel block}} = height\ of\ steel\ block = 37$ mm

$l_{\text{Yoke}} = height\ of\ yoke = 110$ mm

$l_{\text{PM}} = thickness\ of\ PM = 5$ mm

$l_{\text{Steel plate}} = half\ of\ the\ plate\ thickness \times 2$

$+ Average\ of inner\ and\ outer\ radius\ of\ yoke = 110$ mm

$A_{\text{air}} = \pi(outer\ radius\ of\ yoke)^2 - \pi(inner\ radius\ of\ yoke)^2 = 12566.37\ \text{mm}^2$

$A_{\text{MRE}} = \pi(radius\ of\ MRE)^2 = 7853.98\ \text{mm}^2$

$A_{\text{Steel sheet}} = \pi(radius\ of\ steel\ sheet)^2 = 7853.98\ \text{mm}^2$

$A_{\text{Steel block}} = \pi(radius\ of\ steel\ block)^2 = 7853.98\ \text{mm}^2$

$A_{\text{Yoke}} = \pi(outer\ radius\ of\ yoke)^2 - \pi(inner\ radius\ of\ yoke)^2 = 12566.37\ \text{mm}^2$

$A_{\text{PM}} = \pi(radius\ of\ PM)^2 = 7853.98\ \text{mm}^2$

$A_{\text{Steel plate}} = (plate\ thickness) \times \pi(diameter\ of\ steel\ block$

$+ inner\ diameter\ of\ yoke)/2 = 4398.23\ \text{mm}^2$

Appendix B

Reluctance of fringing path

	l (m)	A (m^2)	R (Aturns/Wb)
R_{air1}	6.57E-03	3.14E-04	1.66E+07
R_{air2}	1.29E-02	3.14E-04	3.25E+07
R_{air3}	1.91E-02	3.14E-04	4.84E+07
R_{air4}	2.54E-02	3.14E-04	6.43E+07
R_{air5}	3.17E-02	3.14E-04	8.02E+07
R_{air6}	3.80E-02	3.14E-04	9.62E+07
R_{air7}	4.43E-02	3.14E-04	1.12E+08
R_{air8}	5.06E-02	3.14E-04	1.28E+08
R_{air9}	5.68E-02	3.14E-04	1.44E+08